



The effect of charging conditions on hydrogen embrittlement behavior of ultra-high-strength steel 22MnB5

Yi Liu ^a, Yang Chen ^a, Chendong Yang ^a, Junhe Lian ^b, Yi Feng ^c, Xianhong Han ^{a,d,*}

^a National Engineering Research Center of Die & Mold CAD and State Key Laboratory of Metal Matrix Composites, Shanghai Jiao Tong University, 200240 Shanghai, PR China

^b Advanced Manufacturing and Materials, Department of Mechanical Engineering, Aalto University, 02150 Espoo, Finland

^c China Automotive Engineering Research Institute Co. Ltd, Chongqing 401122, China

^d Institute of Forming Technology & Equipment, School of Materials Science and Engineering, Shanghai Jiao Tong University, Shanghai 200240, China

ARTICLE INFO

Keywords:

Hot-stamping steel 22MnB5
Hydrogen embrittlement
Charging conditions
Reversibility
Hydrogen micropoint technique

ABSTRACT

The effect of charging conditions on hydrogen embrittlement (HE) of the hot-stamping boron steel was investigated with its hydrogen distributions and reversibility properties. With low hydrogen concentration, no noticeable hydrogen-induced cracking was detected, coupled with the uniform distributed diffusible hydrogen, realizing reversible HE. The quasi-cleavage fracture modes suggested the hydrogen-enhanced localized plasticity (HELP) mechanism. At high hydrogen concentration, the diffusible hydrogen distributed at the martensitic block and prior austenite grain boundaries which facilitated hydrogen-induced cracking initiation and propagated along the {110}_M plane, leading to irreversible HE. The intergranular fracture modes suggested the transition of HELP to hydrogen-enhanced decohesion mechanism (HEDE).

1. Introduction

Ultra-high-strength steel parts produced by the hot stamping process, also named press hardening steel (PHS), are widely utilized in automotive industries due to their high strength and reduced weight. Hot stamping technology utilizes the high formability of austenite at elevated temperatures, and simultaneously, achieves ultra-high strength due to the as-quenched martensitic structure of the hot-stamped products [1]. However, hot-stamped steel is vulnerable to suffering the high hydrogen embrittlement sensitivity due to its high strength and martensitic structure [2,3]. Hydrogen embrittlement (HE) is caused by the diffusion of hydrogen atoms in steel which is mainly introduced in the manufacturing process and in-service conditions [4,5]. In general, the external acidic environment or hydrogen gas atmosphere provides the hydrogen atoms by reduced hydrogen ions and dissociated hydrogen gas, respectively. Then, the hydrogen atoms adhere to the surface of the steel, and subsequently, ingress into the substrate through physisorption, chemisorption, diffusion, etc. Consequently, with the presence of hydrogen atoms, the external stress below the yield strength of the steel can result in unexpected catastrophic failures. In laboratory scale, the cathodic hydrogen charging is adopted to simulates the industrial

procedure. Therefore, the charging current density is an essential parameter to investigate hydrogen embrittlement behavior. For instance, Laureys et al. [6] illustrated that the effect of charging current density on the cracking behavior of a material, i.e. the higher current density facilitated the shape-changing of blister and promoted the transition of transgranular (low current density) to intergranular fracture. Liu et al. [7] reported that the charging current density can affect the coating condition of aluminized 22MnB5 steel, thereby resulting in different hydrogen embrittlement sensitivity. Thus, a deep and thorough understanding of the foundation mechanism of hydrogen-induced fractures is very essential for developing ultra-high-strength steels with lower hydrogen embrittlement sensitivity.

The microstructure characterization reveals the PHS is mainly composed of a martensitic structure after hot stamping. The martensitic phase usually shows a hierarchical structure with three different length-scale units [8], i.e., lath, block, and packet which are contained in one prior austenite grain. The martensite lath, with a thickness of about 0.2 μm [9], is considered as the smallest structural unit of martensite. Notably, the misorientation between two of the laths boundaries is $<3^\circ$ which is hardly distinguished in the grain boundary map. The aggregation of lath bundles with nearly the same crystallographic orientation

* Corresponding author at: National Engineering Research Center of Die & Mold CAD and State Key Laboratory of Metal Matrix Composites, Shanghai Jiao Tong University, 200240 Shanghai, PR China.

E-mail address: hanxh@sjtu.edu.cn (X. Han).



promotes the formation of a block. Similarly, several blocks with nearly the same habit plane ($\{111\}_\gamma$) form a packet structure. Due to four different $\{111\}_\gamma$ planes in one prior austenite grain, the coexistence of several packets could be observed. Generally, there are two typical hydrogen-related fracture modes related to boundaries in martensitic steels, i.e., the quasi-cleavage and intergranular fracture. Normally, the quasi-cleavage cracking occurs on the $\{110\}$ planes of martensite and propagates in a transgranular manner [10,11]. Shibata et al. [10] reported that hydrogen-enhanced local dislocation slips resulted in the formation and propagation of cracking along $\{110\}_M$ plane which caused the quasi-cleavage fracture along the lath/block boundaries. In addition, hydrogen-related quasi-cleavage fracture along the $\{110\}_M$ planes was also confirmed in ferritic steel [12]. It indicated that the cracking initiation and propagation along $\{110\}$ planes were an intrinsic characteristic of hydrogen-related fracture in body-centered cubic (BCC) structural metals regardless of the microstructures. On the other hand, the hydrogen-related intergranular fracture in martensitic steel was mainly detected at prior austenite grain boundaries [13]. Shibata et al. [13] investigated the hydrogen-related fracture behavior in martensitic steel and illustrated that the higher hydrogen content facilitated the initiation and propagation of hydrogen-induced cracking along the prior austenite grain boundaries.

The fractography analysis of martensitic steel provides a simple and visualized method to investigate the hydrogen effect on mechanical properties. Nonetheless, the diffusion behavior of hydrogen has not been revealed and outlined, since diffusible hydrogen is tricky to trace by conventional experimental techniques. The hydrogen microprint technique (HMT) which is a method to visualize the distribution of diffusible hydrogen according to the reduction reaction between silver ion (Ag^+) and hydrogen atoms (H) emitted from the specimen, has been widely adopted. For instance, Momotani et al. [14,15] using the HMT method revealed the diffusible hydrogen accumulation behavior of martensitic steels with different strain rates, i.e., a lower strain rate facilitated diffusible hydrogen to mainly accumulating at prior austenite grain boundaries. Pu et al. [16] investigated the movement of hydrogen within an austenitic stainless steel by the HMT method and illustrated that dislocations act as trap sites and trapped hydrogen atoms move with them during plastic deformation. Moreover, with the help of the HMT method Allen et al. [17] visualized the hydrogen behavior during the recovery of mechanical properties, i.e., hydrogen desorption through grains with $\langle 001 \rangle$ and $\langle 101 \rangle$ orientation faster than grains with $\langle 111 \rangle$ orientations.

Although the hydrogen embrittlement mechanism of ultra-high-strength martensitic steel has been actively studied, the reversibility of hydrogen embrittlement has not been exhaustive reported. In the present work, we adopted the hot stamping steel (22MnB5) which is widely used in actual industrial, subjected to slow strain rate tensile (SSRT) tests after electrochemical hydrogen charging. Then, the relationship between hydrogen concentration and fracture modes and hydrogen-induced cracking was evaluated through a scanning electron microscope (SEM) and electron backscattering diffraction (EBSD) technology. The HMT test was conducted which effectively visualized the accumulated behavior of hydrogen atoms at various martensitic boundaries under different hydrogen concentrations. Consequently, the visualization of hydrogen distribution and accumulation plays a decisive role to illustrate the reversibility of hydrogen embrittlement.

2. Experiments

The hot stamping 22MnB5 steel (thickness of 1.4 mm) produced by Baosteel Co. was prepared for current research. The microstructure of the as-received steel (before hot stamping) was composed of ferrite and pearlite. Then, the as-received steel was subjected to austenitize at 920 °C for 5 min and followed by water quenching. Thus, a fully martensitic microstructure can be obtained.

Flat dog-bone-shaped tensile specimens with a gauge section of 16

(length) \times 6 (width) \times 1.4 (thickness) mm³ were cut along the rolling direction from the austenitize-treated steels according to GB/T 228.1-2010, ground with SiC paper (up to 2000#) to remove any surface damage. Then, the specimen was subjected to electrochemical hydrogen charging in a 0.5 mol/L diluted H₂SO₄ electrolyte containing 1 g/L thiourea. Two types of charging current densities were designed, i.e., 0.001 A (0.521 mA/cm²) and 0.1 A (52.1 mA/cm²) for varying charging times. After hydrogen charging, the SSRT tests of the specimen were conducted in Zwick/Roell Z100 testing machine. The strain rate is 10⁻⁴ s⁻¹, i.e., the crosshead displacement rate is 0.096 mm/min. Notably, the crosshead displacement is selected for precisely reflecting the sample's deformation when the strain is very small. The strain can be approximately evaluated by crosshead displacement, as the following formula:

$$\varepsilon = \frac{d_{CD}}{l_0} \times 100\% \quad (1)$$

where ε is strain, d_{CD} is crosshead displacement and l_0 is gauge length (16 mm). At least three measurements were performed for each charging condition to check the repeatability of the results. Then, the hydrogen embrittlement susceptibility index of each specimen was evaluated as following formulas:

$$\sigma_{loss} = \frac{\sigma_{Air} - \sigma_{Hydrogen}}{\sigma_{Air}} \quad (2)$$

$$d_{loss} = \frac{d_{Air} - d_{Hydrogen}}{d_{Air}} \quad (3)$$

The σ_{Air} and d_{Air} are tensile strength and crosshead displacement of an uncharged specimen, respectively. The $\sigma_{Hydrogen}$ and $d_{Hydrogen}$ are tensile strength and crosshead displacement of a hydrogen-charged specimen, respectively.

To analyze the crystallographic features of the hydrogen-related cracking, the hydrogen-charged specimens were prepared by electro-polishing in a solution of 10% HClO₄ + 90% CH₃COOH at a voltage of 20 kV. Then, the crystallographic orientations were characterized by EBSD attached to a scanning electron microscope (Tescan Mira3) equipped with a field emission gun and operated at 20 kV. Additionally, the SEM analysis was performed to investigate the characteristic of the fracture surface and hydrogen microprint specimen. For SEM characterizing, the specimens were etched with a 4% nitric acid alcohol solution.

Hydrogen accumulation behavior under different charging conditions was evaluated visually by the HMT method. The specimens were hydrogen-charged after being etched with a 4% nitric acid alcohol solution. Then, the hydrogen-charged specimen was covered with a liquid emulsion containing AgBr and Na₂NO₂ by wire loop methods. The process lasted for 16 h to make the reaction fully carried out. The AgBr was reduced to Ag particles by diffusible hydrogen atoms according to the following reaction:



Next, the specimen was dipped into a fixing solution, which was composed of Na₂S₂O₃ + Na₂NO₂ (1:1), for 1 h to eliminate the unreacted AgBr emulsion. During the HMT tests, all the procedures were carried out in a dark room to prevent the reaction between AgBr and light.

Moreover, the Image Pro Plus software has been used to quantify the coverage rate of Ag particles on martensite (Ag_M), and the percentages of Ag particles at block boundaries (Ag_{BBs}) and at prior austenite grain boundaries (Ag_{PAGBs}) respectively, as following formulas:

$$\text{Ag}_M = \frac{\text{Ag}_{area} [\mu\text{m}^2]}{\text{Martensite}_{area} [\mu\text{m}^2]} \times 100\% \quad (5)$$

$$\text{Ag}_{BBs} = \frac{\text{Ag}_{area at BBs} [\mu\text{m}^2]}{\text{Ag}_{area} [\mu\text{m}^2]} \times 100\% \quad (6)$$

$$Ag_{PAGBs} = \frac{Ag_{area\ at\ PAGBs}\ [\mu m^2]}{Ag_{area}\ [\mu m^2]} \times 100\% \quad (7)$$

3. Results

3.1. The HE phenomena under different charging current densities

Fig. 1a shows the tensile engineering stress-crosshead displacement curves of the hot-stamped 22MnB5 steel after hydrogen charging with a low current density of 0.001A for varying periods. **Fig. 1b** shows the charging time function of stress and crosshead displacement, and the detailed values have been listed in **Table 1**. Obviously, the strength and crosshead displacement decrease with prolonged charging time. After 2 h charging, the tensile strength (TS) and crosshead displacement (CD) have decreased to 622 MPa and 0.071 mm ($\epsilon = 0.44\%$), i.e., the loss of TS and CD is 62.1% and 93.2%, respectively. Increasing hydrogen charging time to 4 h (Fig. S1), the mechanical properties have no noticeable change, i.e., the TS and CD are 575 MPa and 0.086 mm ($\epsilon = 0.54\%$), respectively. Thus, it is inferred that, after 2 h hydrogen charging, the diffusible hydrogen in the specimen is nearly in dynamic equilibrium. Interestingly, for 8 h hydrogen charging (Fig. S1), a slight increase of the TS (812 MPa) and CD (0.100 mm) have been detected. Combined with the actual hydrogen-charging phenomenon, the slightly increasing can be ascribed to hydrogen bubbles which are formed from the reduction reaction and adhere to the surface of the specimen, thereby reducing the effective region of the reduction reaction.

Fig. 2 illustrates the stress-crosshead displacement curves of the hot-stamped 22MnB5 steel after hydrogen charging with a high current density of 0.1 A for various periods. The detailed mechanical properties are presented in **Table 2**. Obviously, after 0.5 h hydrogen charging, the simultaneous decrease of tensile strength (360 MPa) and CD (0.047 mm) is sluggish which can be confirmed by the similar loss of mechanical properties (σ_{loss} and d_{loss}) between 0.5 h and 1 h hydrogen charging. It indicates that less time (0.5 h) is required to reach a diffusible hydrogen dynamic equilibrium with high-current density (0.1 A). In addition, it is worth noting that the deterioration of mechanical properties (especially strength) in specimens with 0.1 A charging condition is more severe than 0.001 A charging condition.

3.2. The reversibility behavior of PHS after hydrogen charging

To investigate the reversibility behavior of hot-stamped specimens with two different hydrogen-charging conditions, the hydrogen-charged specimens were exposed to the air for varying times which was named storage treatment, and then the SSRT tests were conducted to get the stress-crosshead displacement curves. For low-current saturated hydrogen charging conditions (0.001A-2 h), after a series of storage

Table 1

Mechanical properties of specimens with 0.001A charging current for various charging time.

No.	Charging time (h)	Tensile strength (MPa)	Crosshead displacement (mm)	σ_{loss} (%)	d_{loss} (%)
1	Uncharged	1643	1.050	—	—
2	0.5	1458	0.237	11.3	77.4
3	2	622	0.071	62.1	93.2

treatments, the SSRT tests have been conducted, as shown in **Fig. 3a**. With the extension of storage time, the tensile strength and crosshead displacement present a detectable simultaneous increase (**Figs. 3** and S2). Obviously, with 4 h storage treatment, the tensile strength has been recovered, as the σ_{loss} values in **Table 3**. Especially, after 48 h storage treatment, the mechanical properties were basically recovered as the uncharged specimens, i.e., realized the reversibility of hydrogen embrittlement.

Fig. 4 shows the stress-crosshead displacement curves of specimens with high-current saturated hydrogen charging conditions (0.1A-1 h) after different storage treatments, the detailed values can be found in **Table 4**. Obviously, the hydrogen embrittlement behavior is irreversible with a higher hydrogen charging current density. Specifically, even after 200 h storage treatment, the σ_{loss} and d_{loss} are still showing a high value of 79.6% and 93.6%, respectively. By comparing the mechanical properties of hot-stamped specimens with different hydrogen charging conditions and subsequently storage treatments, it can be clearly found that the diffusible hydrogen leads to deterioration of mechanical properties, which is more severe with higher hydrogen charging current density. Hence, the factor, which results in the irreversible hydrogen embrittlement, will be elucidated in the following investigation.

3.3. The microstructure characterizations for different charging conditions

After SSRT tests, the EBSD images were taken at a depth of several hundred micrometers below the fracture surfaces of the hydrogen-saturated specimens with low (**Fig. 5a**) and high (**Fig. 5b**) current charging, respectively. In band contrast (BC) maps (**Fig. 5a₁-b₁**), it shows the typical martensitic structure which is composed of a three-level hierarchy in its morphology, i.e., lath, block, and packet boundaries. Interestingly, two long and detour hydrogen-induced cracks (red arrows in **Fig. 5b₁**) are only observed in the specimen with a high charging current density. To further confirm the initiation and propagation of cracks, the prior austenite grain boundaries and hydrogen-induced cracks have been outlined by white and black dotted lines in inverse pole figure (IPF) maps (**Fig. 5b₂**), respectively. It can be clearly observed

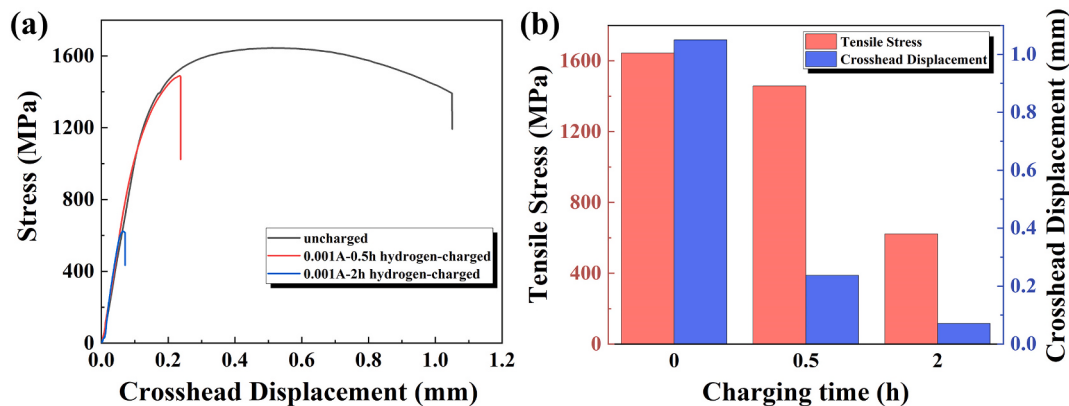


Fig. 1. (a) Stress-crosshead displacement curves of the hot-stamped specimen after hydrogen charging with 0.001A for varying time. (b) Charging time as a function of tensile stress and crosshead displacement.

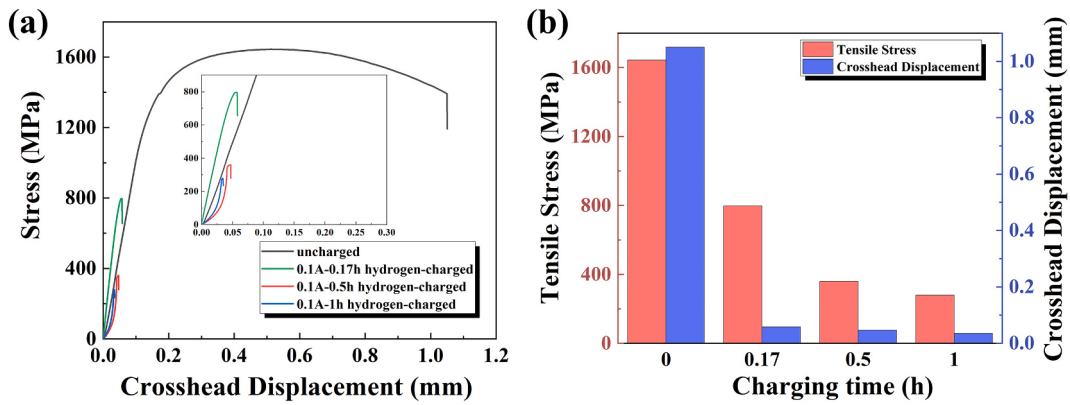


Fig. 2. Stress-crosshead displacement curves of the hot-stamped specimen after hydrogen charging with 0.1 A for various time. (b) Comparison of mechanical properties.

Table 2

Mechanical properties of specimens with 0.1 A charging current for various charging time.

No.	Charging time (h)	Tensile strength (MPa)	Crosshead displacement (mm)	σ_{loss} (%)	d_{loss} (%)
1	Uncharged	1643	1.05	—	—
2	0.17	797	0.058	51.5	94.5
3	0.5	360	0.047	78.1	95.5
4	1	279	0.035	83.0	96.7

that two types of cracks exist simultaneously, i.e., the crack propagates along with prior austenite grain boundaries (as indicated by the black arrows in Fig. 5b₂) causing the intergranular cracking, then crosses through the prior austenite grain and nearly parallels to the growth direction of the martensitic block (as indicated by the white arrows in Fig. 5b₂) which results in transgranular cracking. Moreover, the traces of {110} planes near the cracks have been portrayed by black lines (Fig. 5b₂). Surprisingly, the {110}_M planes are nearly paralleled to the cracks propagating path. Contrastively, there is no crack in the low-current hydrogen-charged specimen which shows a random distribution of crystallographic orientation (Fig. 5a₂). In Fig. 5a₃-b₃, the kernel average misorientation (KAM) maps show the changing of local misorientation caused by geometrically necessary dislocations, and to some extent reflect the local dislocation density. The higher KAM values are found along block boundaries, which suggested that these boundaries have high dislocation densities and are susceptible to crack propagation.

To precisely reveal the crystallographic features of the crack propagation direction in the specimen with high-current hydrogen charging,

the relationship between the cracking path and {110}_M planes has been examined in Fig. 6. Crystallographic orientation analysis reveals that the cracking propagation direction indicated by the black lines in Fig. 6b is parallel to the {011}_M plane trace which can be proven by the corresponding pole figure (red dot in Fig. 6d). In BCC-structured martensite, the slip system is <111> {011} [18]. Thus, it suggests that the accumulation of dislocations in {110} planes results in the formation of cracking, as confirmed by the high KAM values in Fig. 6c. It's noteworthy that the cracking path is basically parallel to the block boundary of the lath martensite structure (Fig. 6a).

To confirm the crack in Figs. 5b and 6 is caused by the diffusible hydrogen rather than tensile stress. The microstructure of the high-current density charged specimen before SSRT tests have been examined. In Fig. 7, the prior austenite grain boundaries have been outlined by white dotted lines. Two types of hydrogen-induced cracking can be distinguished, i.e., intergranular cracking (Fig. 7a) and transgranular cracking (Fig. 7b). In addition, the propagation of the transgranular cracking is parallel to the block boundaries.

Table 3

Mechanical properties of specimens with 0.001A-2 h charging condition for different storage treatments.

No.	Storage time (h)	Tensile strength (MPa)	Crosshead displacement (mm)	σ_{loss} (%)	d_{loss} (%)
1	Uncharged	1643	1.050	—	—
2	0	622	0.073	62.1	93.0
3	4	1654	0.906	0	13.7
4	48	1656	1.030	0	1.9

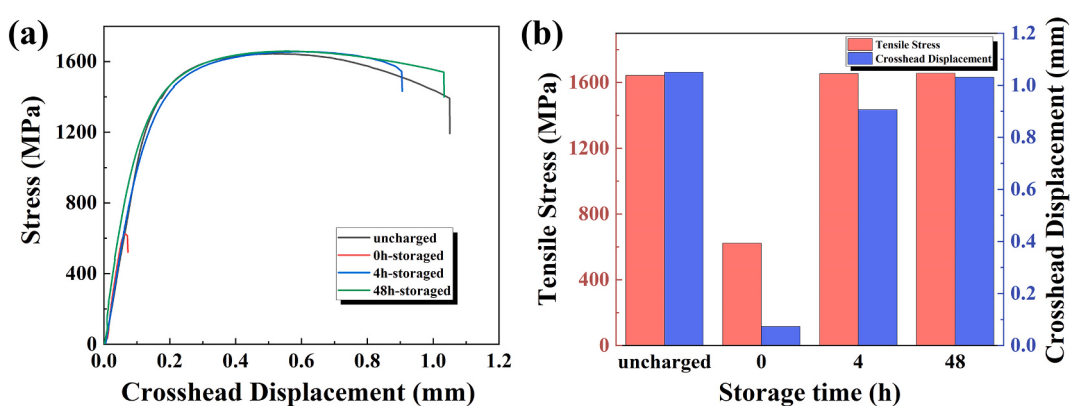


Fig. 3. (a) Stress-crosshead displacement curves of the low-current saturated hydrogen-charged specimen after different storage treatments. (b) Comparison of mechanical properties.

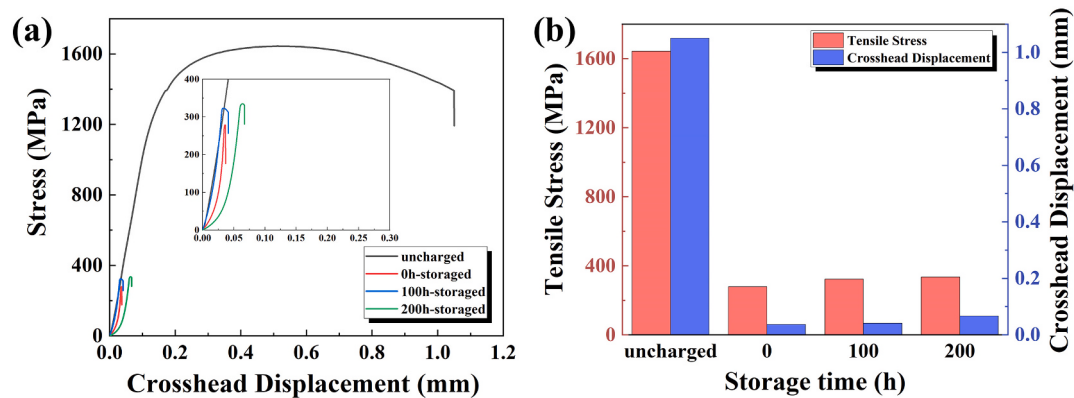


Fig. 4. (a) Stress-crosshead displacement curves of specimens with high-current saturated hydrogen-charged after different storage treatments. (b) Comparison of mechanical properties.

Table 4

Mechanical properties of the 0.1A-1 h hydrogen-charged steel with different storage treatments.

No.	Storage time (h)	Tensile strength (MPa)	Crosshead displacement (mm)	σ_{loss} (%)	d_{loss} (%)
1	Uncharged	1643	1.05	—	—
2	0	279	0.037	83.0	96.5
3	100	323	0.041	80.3	96.1
4	200	335	0.067	79.6	93.6

Detailed fractography analysis was carried out on the specimen using SEM after the SSRT testing to investigate the fracture mechanism, and the results are shown in Fig. 8. Obviously, the uncharged specimen is subjected to local necking before fracture (red dotted lines in Fig. 8a₁). The center of the fracture surface is dominated by micro-void coalescence fracture mode (Fig. 8a₂), and the shallow dimples are prevailing at the edge of the fracture surface (Fig. 8a₃), which means that ductile fracture occurs with sufficient deformation. However, in the hydrogen-charged specimens, the dimples are replaced by brittle fracture features. It is easily recognizable that with hydrogen charging, the fracture surface appears flatter (Fig. 8b₁-c₁). With low current density hydrogen charging, the center of the fracture surface is occupied by a mixture feature of intergranular cracking (white arrows in Fig. 8b₂) and quasi-

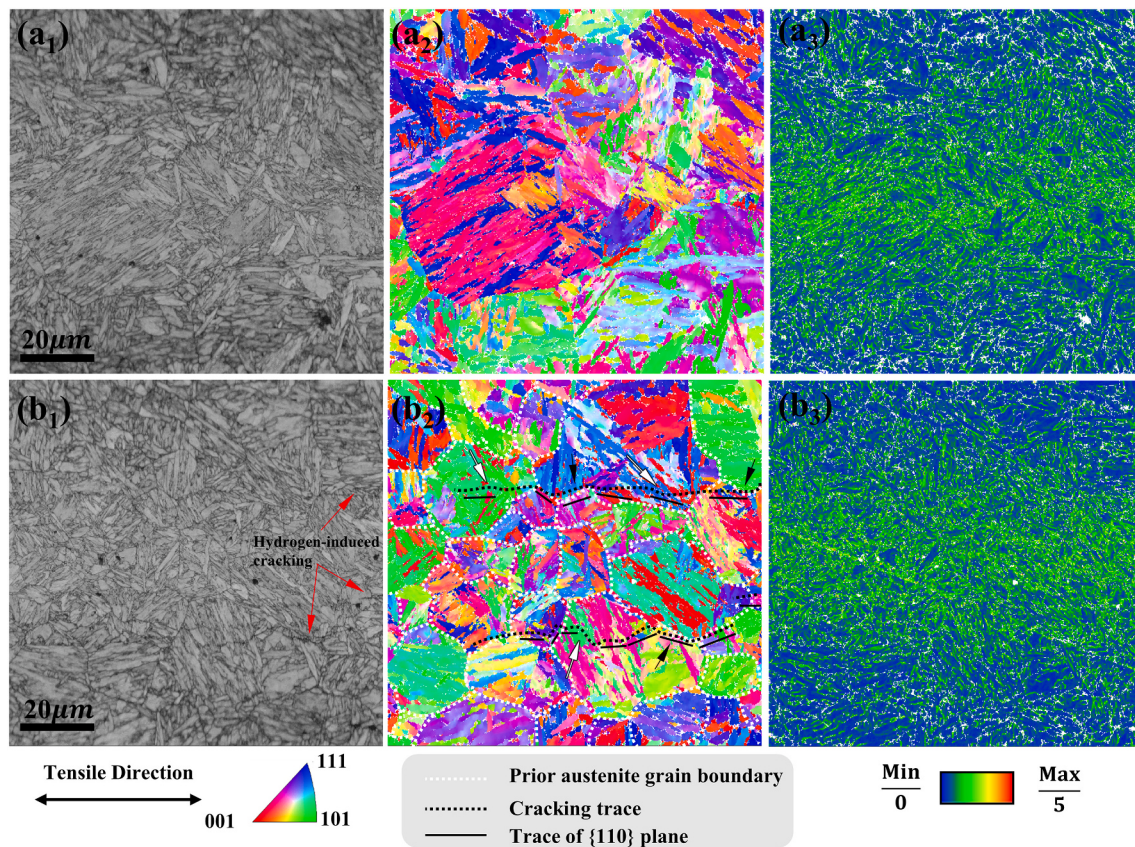


Fig. 5. EBSD images in the vicinity of fracture surfaces of (a) 0.001A-2 h and (b) 0.1A-1 h hydrogen-charged specimen, including (a₁-b₁) band contrast (BC) maps; (a₂-b₂) inverse pole figure (IPF) maps and (a₃-b₃) kernel average misorientation (KAM) maps.

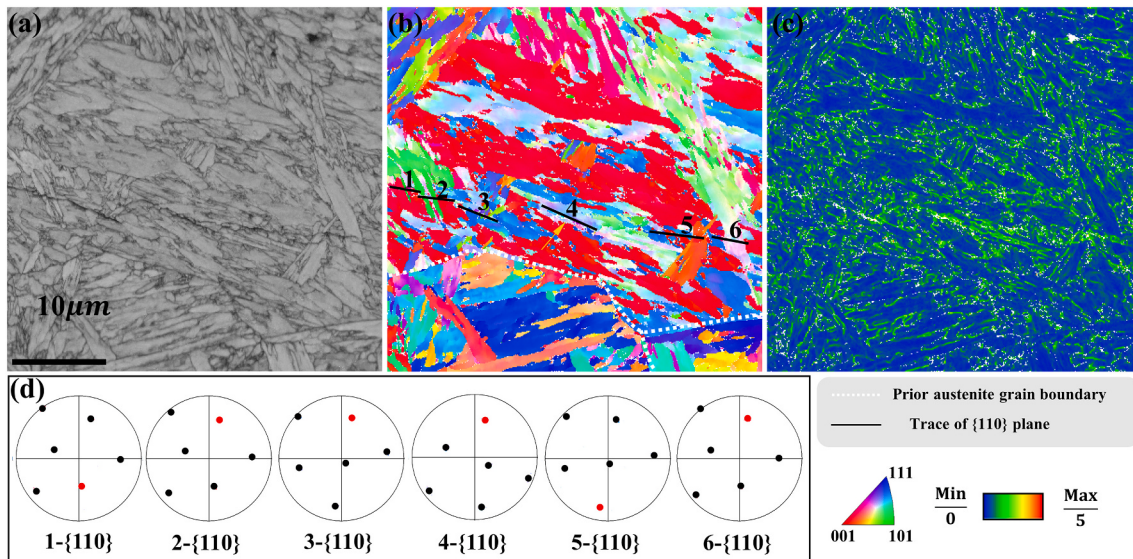


Fig. 6. The hydrogen-induced cracking in the specimen with 0.1A-1 h charging condition. (a) BC map, (b) IPF map, (c) KAM map, (d) {110} pole figures correspondence to (b).

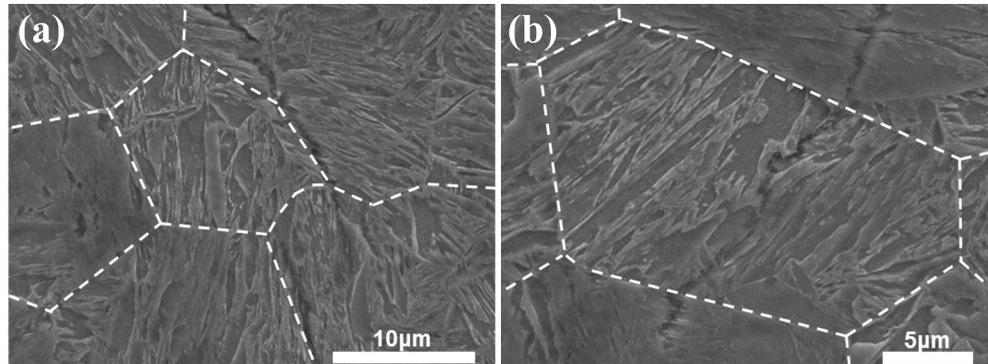


Fig. 7. Two types of hydrogen-induced cracking in the specimen with 0.1A-1 h hydrogen charging. (a) intergranular cracking, (b) transgranular cracking.

cleavage facet. For the edge of the fracture surface (Fig. 8b₃), the river-like pattern decorated quasi-cleavage fracture mode is dominant. With increasing the current density, transgranular cracking is detected at the edge of the fracture surface (yellow arrows in Fig. 8c₃). Also, the arc-like deep cracking, which enlarged images show in the insert figure, is detected in the region that is close to the surface of hydrogen charging (yellow arrows in Fig. 8c₁). Moreover, in the inner of the fracture surface, the deeper and more severe intergranular cracking (white arrows) with smooth facets (red arrows) has been observed (Fig. 8c₂).

3.4. Hydrogen distribution visualized by HMT

To visualize the hydrogen accumulation behavior under different charging conditions, the HMT was adopted. Fig. 9a and b-c show the SEM images of the uncharged and hydrogen-charged specimens after HMT treatments, respectively. Table 5 quantifies the proportion of Ag particles on martensite, block and prior austenite grain boundaries. In the absence of hydrogen, Fig. 9a shows a typical lath martensite structure without any Ag particles. Accordingly, it confirms that the Ag particles are displaced by the hydrogen provided by electrochemically hydrogen charging. With low-current density hydrogen charging, Ag particles are mostly randomly distributed in the martensitic block boundaries (Fig. 9b), while a tiny portion (15.67%) is located at prior austenite grain boundaries (red arrows in Fig. 9b). Thus, it indicates that the diffusible hydrogen basically presents homogeneous distribution

under low-current density charging. While, after high-current density hydrogen charging, the amount of Ag particles shows a noticeable increase (Fig. 9c₁), i.e. from 0.86% to 5.24% (Table 5). It is worth noting that, the precipitation of Ag particles along various boundaries in the martensitic structure, such as block boundaries and prior austenite grain boundaries. Specially, parts of Ag particles precipitate along the growth direction of block boundaries (red dotted arrow in Fig. 9c₁) which promotes the formation of transgranular cracking, as confirmed in Fig. 7b. Moreover, the distribution of Ag particles has been detected at the triple junction boundaries of prior austenite grain boundaries (Fig. 9c₂), thereby leading the increased proportion of Ag particales at prior austenite grain boundaries (26.14%). Then, the accumulated hydrogen atoms at the triple junction boundaries facilitate the initiation of intergranular cracking which is consistent with the observation in Fig. 7a.

The HMT treatments were also conducted on the specimens with storage treatment. After low-current density hydrogen charging and 48 h storage treatment, the HMT results show the absence of Ag particles inside the martensite (Fig. 10a), i.e., entire hydrogen emission occurs. Theoretically, as the hydrogen outgassing, the recovery of mechanical properties can be realized, confirmed in Fig. 3 and Table 3. For specimens with high-current density hydrogen charging and 200 h storage treatment, the Ag particles have nearly disappeared (Fig. 10b), i.e., hydrogen has thoroughly escaped from martensite. Moreover, the hydrogen blister, which results in the formation of cracks, has been

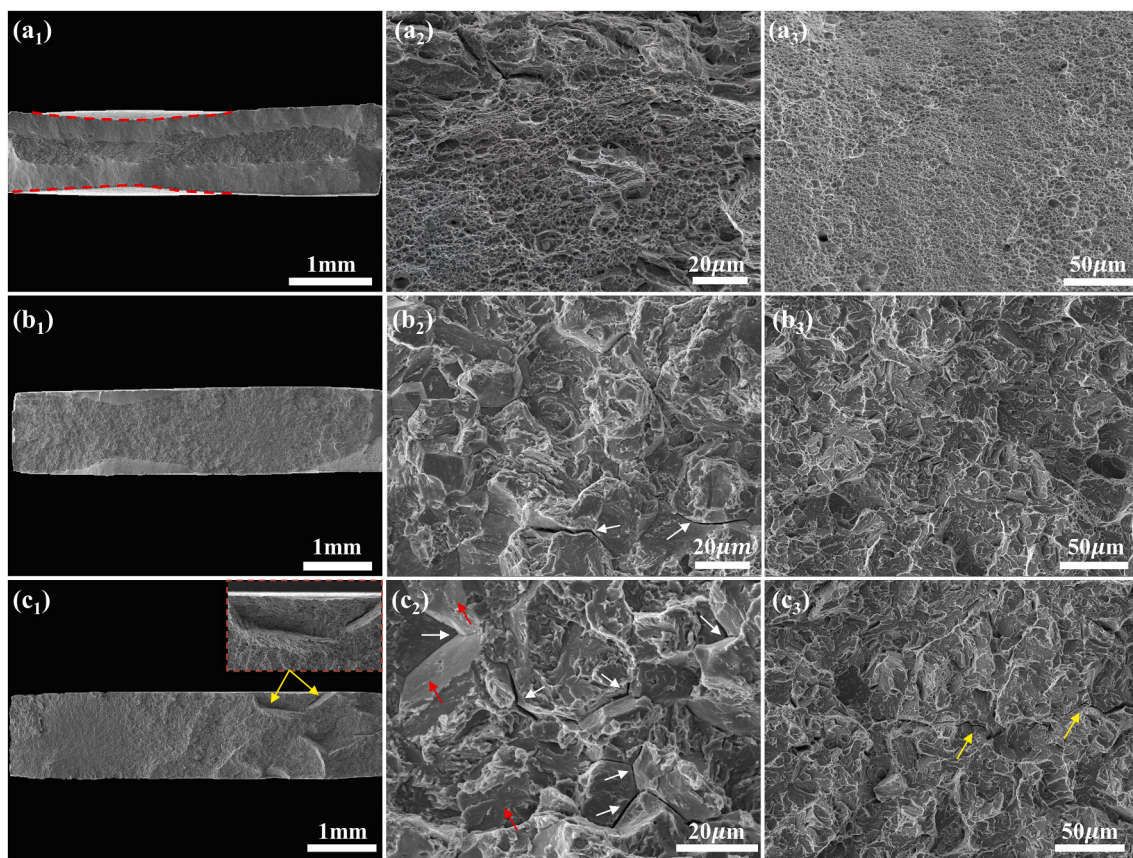


Fig. 8. Fractography of the specimens (a) without and with (b-c) hydrogen charging: (b) 0.001A-2 h; (c) 0.1A-1 h.

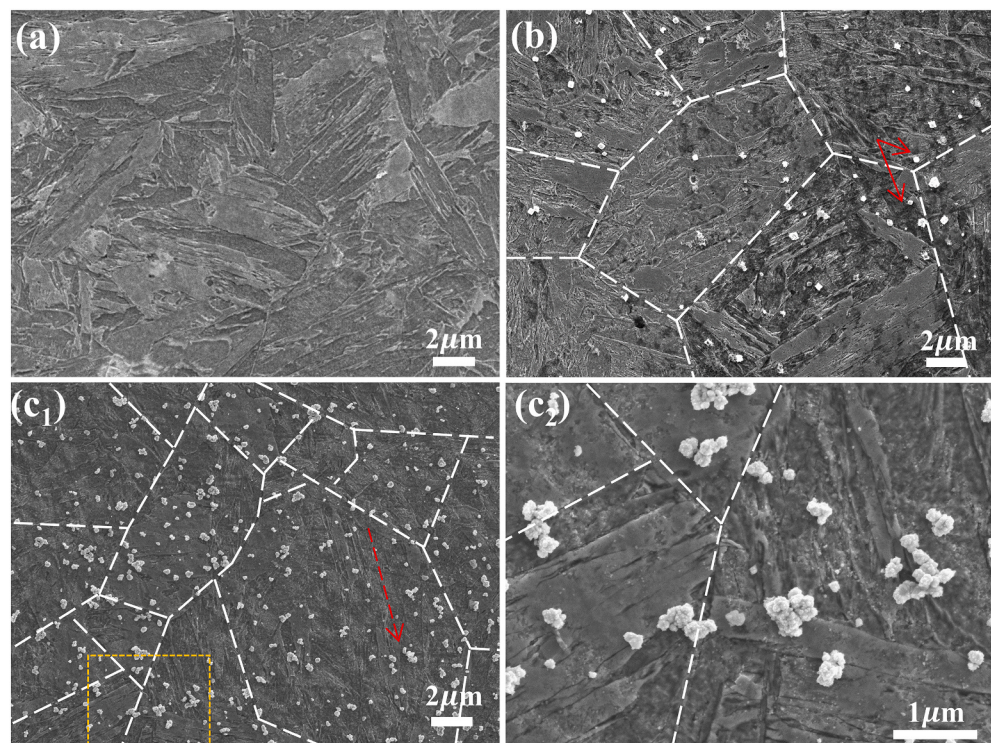


Fig. 9. SEM images of the specimen with HMT treatment. (a) specimen without hydrogen-charging; (b) 0.001A-1 h; (c) 0.1A-1 h.

Table 5

Statistics of precipitation of Ag particles on martensite, at block and prior austenite grain boundaries (PAGBs).

Hydrogen charging current (A)	Ag particles coverage rate on martensite	Percentage at block boundaries	Percentage at PAGBs
0.001	0.86%	52.21%	15.67%
0.1	5.24%	57.39%	26.14%

observed at the edge of the specimen. Thus, the specimen shows irreversible hydrogen embrittlement (Fig. 4 and Table 4).

4. Discussions

Based on the results of experimental research, Fig. 11 illustrates the distribution of diffusible hydrogen and the hydrogen-induced cracking under different charging conditions. After low-current density hydrogen charging, the diffusible hydrogen is randomly dispersed in martensitic block boundaries (Fig. 11a₁), which is an indication of the uniform distribution of hydrogen atoms. The fracture morphology is dominated by quasi-cleavage facets (Fig. 8b) which are verified not the true cleavage planes. Generally, the quasi-cleavage facets are considered the evidence that hydrogen embrittlement is driven by hydrogen enhanced localized plasticity (HELP) mechanism [19,20]. Nagao et al. [21] investigated the role of hydrogen in martensitic steel, and subsequently, elaborated that hydrogen-enhanced dislocation promoted the formation of quasi-cleavage fracture. In addition, Cho et al. [18] carefully investigated the hydrogen-induced quasi-cleavage facet in 22MnB5 steel and illustrated that the fracture mode of quasi-cleavage is ascribed to dislocation movement. Furthermore, a little portion of intergranular

cracking (Fig. 8b₂) can be rationalized as the HELP mechanism increased the mobility and dislocation density around the prior austenite grain boundaries, which can modify the structure of boundaries [21]. Specifically, the increase of dislocation density effectively strengthens the matrix and forms high local stress which facilitates hydrogen accumulation at the prior austenite grain boundaries, thereby reducing the cohesive energy of boundaries. Accordingly, it can be inferred that hydrogen promotes the movement of dislocation (Fig. 11a₁) which leads to the quasi-cleavage fracture. In addition, the piled-up dislocation at prior austenite grain boundaries (Fig. 11a₁) results in a small number of intergranular fracture. Consequently, these experimental observations indicate that the hydrogen embrittlement failure mechanism of the low-current density hydrogen-charged specimen is dominated by the HELP mechanism. Moreover, the tensile tests of the hydrogen-charged specimens with different storage treatments have been conducted to investigate the reversibility of hydrogen embrittlement under low-current density hydrogen charging. The mechanical properties of the hydrogen-charged specimen were recovered after 48 h exposure to air, as diffusible hydrogen diffused out of the specimen (Fig. 11a₂). It can be reasoned as the as-quenched martensite whose inherent microstructure provides the trapping sites for diffusible hydrogen, as confirmed by the work of Verbeken et al. [22]. According to the distribution of hydrogen (Fig. 11a₁), it can be observed that the dominated hydrogen traps are block boundaries which can be regarded as reversible traps. Therefore, based on the definition of reversible traps, i.e., hydrogen atoms are highly possible to emission out before a local hydrogen saturation is achieved [23]. It can be concluded that without the interference of added factors, such as continuous hydrogen charging or applied stress, etc., the hydrogen desorption from the specimen occurs after exposure to air for enough time.

After high-current density hydrogen charging, the fracture mode of

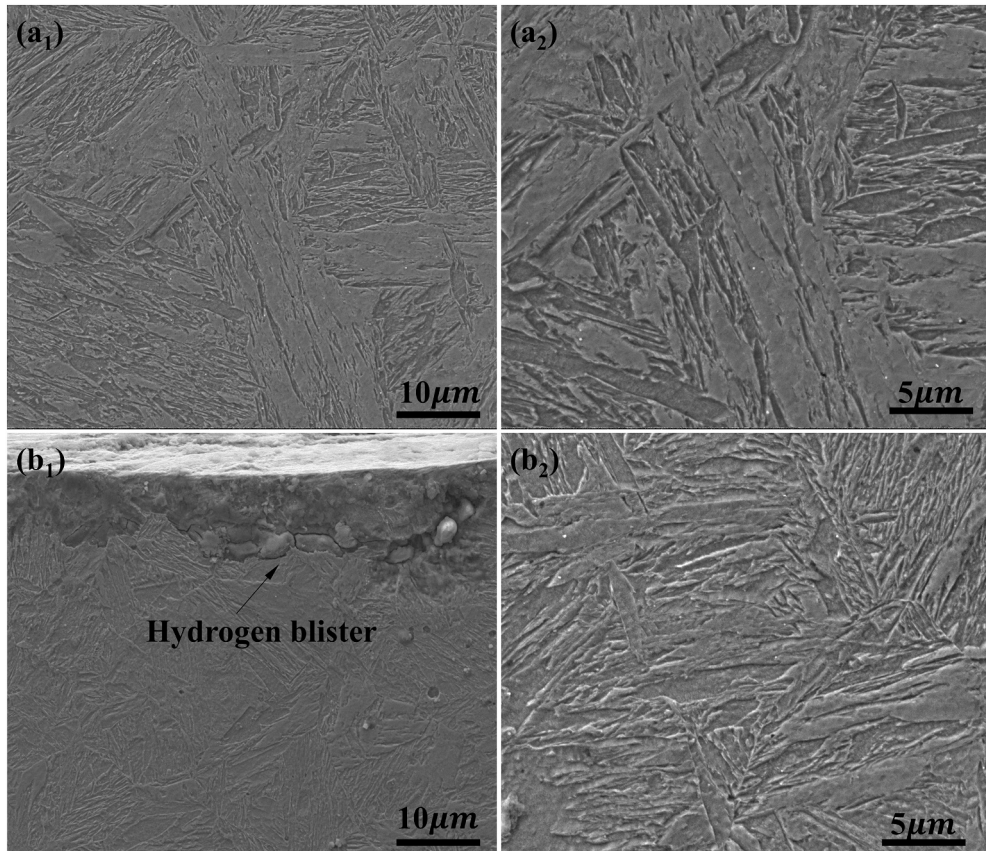


Fig. 10. SEM images of the storage treatment specimen after HMT treatment. (a) 0.001A-2 h hydrogen-charged with 48 h storage; (b) 0.1A-1 h hydrogen-charged with 200 h storage.

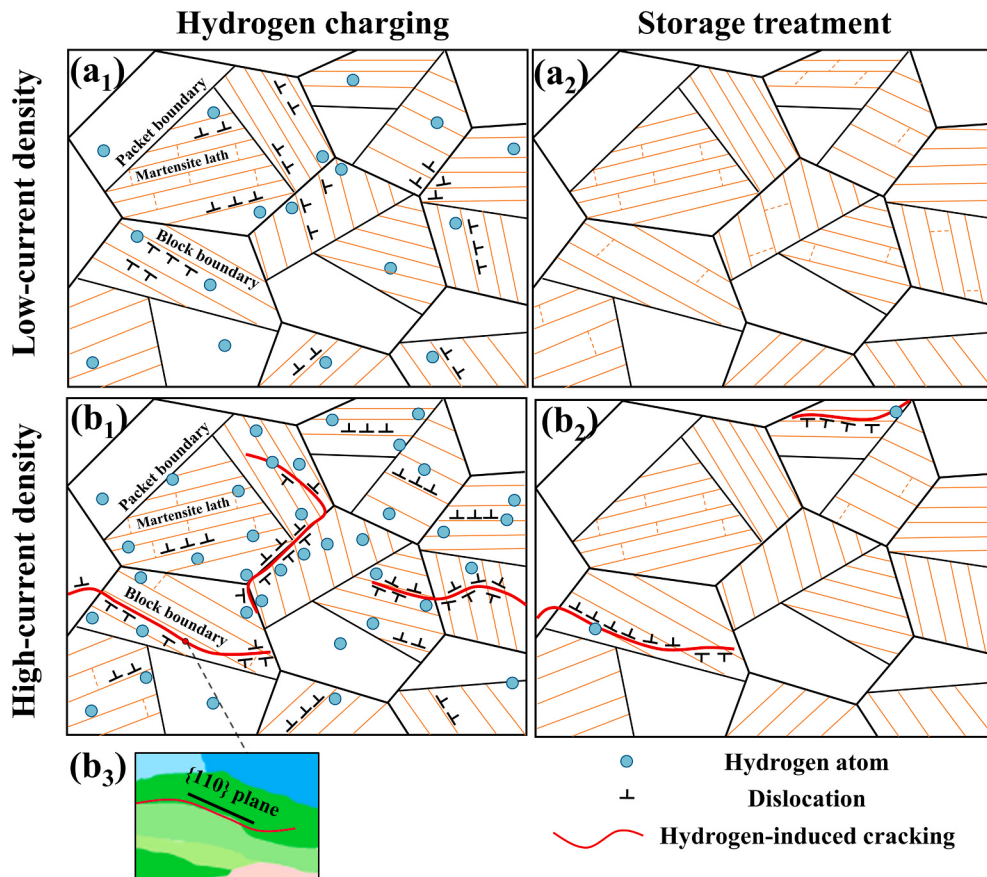


Fig. 11. A schematic sketch of the diffusion and distribution of hydrogen atoms with different hydrogen charging densities under different conditions. (a) 0.001A; (b) 0.1A.

the specimen presents a mixture of intergranular and transgranular fractures (Fig. 8c). The brittle intergranular cracking, which featured smooth facets, and cracking propagating along grain boundaries, was evidence of the hydrogen-enhanced decohesion (HEDE) mechanism [24], i.e., hydrogen decreases the cohesive strength between grain boundaries and results in cracking of these boundaries. In fact, hydrogen atoms have been observed at various boundaries (Fig. 11b₁), especially martensitic block boundaries and prior austenite grain boundaries. Hence, the excessive hydrogen atoms, which accumulate along the growth direction of block boundaries (Fig. 11b₂), weaken the atomic binding energy between the block boundaries and facilitate the formation of cracking. Moreover, the cracking initiates from the prior grain boundaries and propagated in a transgranular manner (Fig. 11b₂), which is also confirmed by Shibata et al. [25]. Momotani et al. [15] illustrated that diffusible hydrogen preferred to accumulate at prior austenite grain boundaries during tensile deformation and led to brittle fracture on or in the vicinity of prior austenite grain boundaries. In addition, the precise crystallographic orientation analyses reveal that the cracking path in high-current density hydrogen charging was parallel to {110}_M planes (Fig. 11b₃). It has been widely accepted that the path of the crack which is parallel to {110}_M planes is induced by hydrogen charging [10,26]. The SEM results (Fig. 7) confirm the formation of cracking before tensile tests. Thus, we can infer that, due to the existence of hydrogen-induced cracking (Fig. 11b₂), the mechanical properties of the hydrogen-charged specimen which was exposed to air for plenty of time still cannot be fully recovered.

The formation of cracks can be reasoned as the local high hydrogen concentration. According to the following equation [27,28]:

$$C_L = \frac{\varphi_0 N_a}{D_0} \exp\left(\frac{-8000}{RT}\right) \sqrt{i_c} \quad (8)$$

where φ_0 is permeation constant; N_a is Avogadro constant; D_0 is diffusion constant; and i_c is charging current density. Obviously, hydrogen concentration (C_L) is proportional to charging density (i_c). A higher current density is related to a higher solubility of hydrogen in the steel [29]. Thus, more hydrogen is simultaneously incorporated into the specimen at higher current densities, which accelerates hydrogen recombination. When the accumulation of hydrogen atoms at a local region reaches the critical hydrogen concentration, the supersaturated hydrogen atoms can recombine into hydrogen molecules because of high binding energy and induce internal pressure during charging [30]. When the internal hydrogen pressure reaches a critical value, it can result in the formation of hydrogen blister (Fig. 10b₁) and the initiation of cracking (Fig. 7) [31]. The related results have been detailed and reported in our previous work [32]. The hydrogen embrittlement mechanism of specimens with different charging conditions can be concluded as follows. For low hydrogen concentration (low-current density), the hydrogen is captured by the high dislocation density decorated block boundaries, due to hydrogen tending to move to the areas with a high-stress concentration [33]. Previous studies [13,34] reported that the slip systems, whose slip planes were parallel to block boundaries, were preferentially operated in martensitic structures. Then, dislocations can transport hydrogen during their motion (e.g., from block interior towards the block boundaries). Thus, hydrogen embrittlement is dominated by the HELP mechanism, i.e., hydrogen can be easily captured by block boundaries and promote local plastic deformation by promoting the movement of dislocation. On the other hand, in martensitic structures, the boundaries, such as block and prior

austenite grain boundaries can act as hydrogen traps, lowering the hydrogen diffusivity [35] and be regarded as the potential high local hydrogen concentration sites, thereby leading to the initiation and propagation of cracking. Thus, with increasing the hydrogen concentration (high-current density), the hydrogen atoms are distributed at block and prior austenite grain boundaries and weaken their cohesive binding energy. Then, the decreased cohesion of grain boundaries results in the HELP mechanism changing to the HEDE mechanism.

5. Conclusions

The effects of charging conditions on hydrogen embrittlement and reversibility of ultra-high-strength 22MnB5 steel were investigated via SSRT testing and the HMT method. The main conclusions were drawn as follows:

- (1) In a low hydrogen concentration situation, diffusible hydrogen was in a dynamic equilibrium after 2 h charging. The fracture morphology of hydrogen embrittlement was composed of quasi-cleavage facets and consistent with the HELP mechanism. In the case of high hydrogen concentration, only 0.5 h charging can achieve dynamic equilibrium. The fracture morphology is an intergranular fracture and secondary cracking consistent with the HEDE mechanism.
- (2) The mechanical properties of the specimen with low hydrogen concentration can be recovered by storage treatments, i.e., hydrogen embrittlement was reversible. However, for specimens with high hydrogen concentration, local high hydrogen concentration facilitates the formation of cracking propagation along {110}_M plane, thereby resulting in irreversible hydrogen embrittlement.
- (3) HMT method was used to characterize the distribution of hydrogen atoms. The results suggested that hydrogen was homogeneously distributed in the martensitic block boundaries at low hydrogen concentration. With a higher hydrogen concentration, hydrogen was prone to distributed at various boundaries (block and prior austenite grain boundaries) of martensite, leading to the formation of cracking.

Declaration of Competing Interest

The authors declare that they have no known competing financial interests or personal relationships that could have appeared to influence the work reported in this paper.

Data availability

No data was used for the research described in the article.

Acknowledgments

This work was supported by the National Natural Science Foundation of China (Grant No. 51775336, 52175349), and the Natural Science Foundation of Shanghai (Grant No. 21ZR1429600). We also thank Ms. Xiaoxin Zhang and Ms. Huizhen Zhang for their support and previous work.

Appendix A. Supplementary data

Supplementary data to this article can be found online at <https://doi.org/10.1016/j.matchar.2022.112377>.

References

- [1] K. Mori, P.F. Bariani, B.A. Behrens, A. Brosius, S. Bruschi, T. Maeno, M. Merklein, J. Yanagimoto, Hot stamping of ultra-high strength steel parts, *CIRP Ann.* 66 (2017) 755–777.
- [2] S.K. Dwivedi, M. Vishwakarma, Effect of hydrogen in advanced high strength steel materials, *Int. J. Hydrog. Energy* 44 (2019) 28007–28030.
- [3] J. Venezuela, F.Y. Lim, L. Liu, S. James, Q. Zhou, R. Knibbe, M. Zhang, H. Li, F. Dong, M.S. Dargusch, A. Atrens, Hydrogen embrittlement of an automotive 1700 MPa martensitic advanced high-strength steel, *Corros. Sci.* 171 (2020), 108726.
- [4] B. Sun, D. Wang, X. Lu, D. Wan, D. Ponge, X. Zhang, Current challenges and opportunities toward understanding hydrogen embrittlement mechanisms in advanced high-strength steels: a review, *Acta Metall. Sin. (Engl.)* 34 (2021) 741–754.
- [5] J. Venezuela, Q. Liu, M. Zhang, Q. Zhou, A. Atrens, A review of hydrogen embrittlement of martensitic advanced high-strength steels, *Corros. Rev.* 34 (2016) 153–186.
- [6] A. Laureys, E. Van den Eeckhout, R. Petrov, K. Verbeken, Effect of deformation and charging conditions on crack and blister formation during electrochemical hydrogen charging, *Acta Mater.* 127 (2017) 192–202.
- [7] Y. Liu, Y. Chen, C. Yang, X. Han, Study on hydrogen embrittlement and reversibility of hot-stamped aluminized 22MnB5 steel, *Mater. Sci. Eng. A* 848 (2022), 143411.
- [8] H. Kitahara, R. Ueji, N. Tsuji, Y. Minamino, Crystallographic features of lath martensite in low-carbon steel, *Acta Mater.* 54 (2006) 1279–1288.
- [9] S. Morito, X. Huang, T. Furuhara, T. Maki, N. Hansen, The morphology and crystallography of lath martensite in alloy steels, *Acta Mater.* 54 (2006) 5323–5331.
- [10] A. Shibata, T. Murata, H. Takahashi, T. Matsuoka, N. Tsuji, Characterization of hydrogen-related fracture behavior in as-quenched low-carbon martensitic steel and tempered medium-carbon martensitic steel, *Metall. Mater. Trans. A* 46 (2015) 5685–5696.
- [11] J. Yoo, S. Kim, M.C. Jo, S. Kim, J. Oh, S.-H. Kim, S. Lee, S.S. Sohn, Effects of Al-Si coating structures on bendability and resistance to hydrogen embrittlement in 1.5-GPa-grade hot-press-forming steel, *Acta Mater.* 225 (2021), 117561.
- [12] K. Okada, A. Shibata, W. Gong, N. Tsuji, Effect of hydrogen on evolution of deformation microstructure in low-carbon steel with ferrite microstructure, *Acta Mater.* 225 (2022), 117549.
- [13] A. Shibata, T. Yonemura, Y. Momotani, M.-h. Park, S. Takagi, Y. Madi, J. Besson, N. Tsuji, Effects of local stress, strain, and hydrogen content on hydrogen-related fracture behavior in low-carbon martensitic steel, *Acta Mater.* 210 (2021), 116828.
- [14] Y. Momotani, A. Shibata, T. Yonemura, Y. Bai, N. Tsuji, Effect of initial dislocation density on hydrogen accumulation behavior in martensitic steel, *Scr. Mater.* 178 (2020) 318–323.
- [15] Y. Momotani, A. Shibata, D. Terada, N. Tsuji, Effect of strain rate on hydrogen embrittlement in low-carbon martensitic steel, *Int. J. Hydrog. Energy* 42 (2017) 3371–3379.
- [16] S.D. Pu, S.W. Ooi, Hydrogen transport by dislocation movement in austenitic steel, *Mater. Sci. Eng. A* 761 (2019), 138059.
- [17] Q.S. Allen, T.W. Nelson, Microstructural evaluation of hydrogen embrittlement and successive recovery in advanced high strength steel, *J. Mater. Process. Technol.* 265 (2019) 12–19.
- [18] L. Cho, P.E. Bradley, D.S. Lauria, M.L. Martin, M.J. Connolly, J.T. Benzing, E.J. Seo, K.O. Findley, J.G. Speer, A.J. Slifka, Characteristics and mechanisms of hydrogen-induced quasi-cleavage fracture of lath martensitic steel, *Acta Mater.* 206 (2021), 116635.
- [19] M.L. Martin, J.A. Fenske, G.S. Liu, P. Sofronis, I.M. Robertson, On the formation and nature of quasi-cleavage fracture surfaces in hydrogen embrittled steels, *Acta Mater.* 59 (2011) 1601–1606.
- [20] E. Merson, A.V. Kudrya, V.A. Trachenko, D. Merson, V. Danilov, A. Vinogradov, Quantitative characterization of cleavage and hydrogen-assisted quasi-cleavage fracture surfaces with the use of confocal laser scanning microscopy, *Mater. Sci. Eng. A* 665 (2016) 35–46.
- [21] A. Nagao, C.D. Smith, M. Dadfarnia, P. Sofronis, I.M. Robertson, The role of hydrogen in hydrogen embrittlement fracture of lath martensitic steel, *Acta Mater.* 60 (2012) 5182–5189.
- [22] D. Pérez Escobar, T. Depover, E. Wallaert, L. Duprez, M. Verhaeghe, K. Verbeken, Thermal desorption spectroscopy study of the interaction between hydrogen and different microstructural constituents in lab cast Fe–C alloys, *Corros. Sci.* 65 (2012) 199–208.
- [23] Y. Sun, Y. Frank Cheng, Hydrogen-induced degradation of high-strength steel pipeline welds: a critical review, *Eng. Fail. Anal.* 133 (2022), 117549.
- [24] S. Zhang, D. Xu, F. Huang, W. Gao, J. Wan, J. Liu, Mitigation of hydrogen embrittlement in ultra-high strength lath martensitic steel via ta microalloying, *Mater. Des.* 210 (2021), 110090.
- [25] A. Shibata, T. Matsuoka, A. Ueno, N. Tsuji, Fracture surface topography analysis of the hydrogen-related fracture propagation process in martensitic steel, *Int. J. Fract.* 205 (2017) 73–82.
- [26] A. Shibata, Y. Momotani, T. Murata, T. Matsuoka, M. Tsuboi, N. Tsuji, Microstructural and crystallographic features of hydrogen-related fracture in lath martensitic steels, *Mater. Sci. Technol.* 33 (2017) 1524–1532.
- [27] J.K. Wu, Electrochemical method for studying hydrogen in iron, nickel and palladium, *Int. J. Hydrog. Energy* 17 (1992) 917–921.
- [28] X. Li, J. Zhang, Y. Wang, B. Li, P. Zhang, X. Song, Effect of cathodic hydrogen-charging current density on mechanical properties of restrained high strength steels, *Mater. Sci. Eng. A* 641 (2015) 45–53.

- [29] T.P. Perng, J.K. Wu, A brief review note on mechanisms of hydrogen entry into metals, *Mater. Lett.* 57 (2003) 3437–3438.
- [30] X.C. Ren, Q.J. Zhou, G.B. Shan, W.Y. Chu, J.X. Li, Y.J. Su, L.J. Qiao, A nucleation mechanism of hydrogen blister in metals and alloys, *Metall. Mater. Trans. A* 39 (2007) 87–97.
- [31] A. Laureys, M. Pinson, T. Depover, R. Petrov, K. Verbeken, EBSD characterization of hydrogen induced blisters and internal cracks in TRIP-assisted steel, *Mater. Charact.* 159 (2020), 110029.
- [32] Y. Chen, Z. Xu, X. Zhang, T. Zhang, J.J. Tang, Z. Sun, Y. Sui, X. Han, Irreversible hydrogen embrittlement study of B1500HS high strength boron steel, *Mater. Des.* 199 (2021), 109404.
- [33] D. Raabe, B. Sun, A. Kwiatkowski Da Silva, B. Gault, H.-W. Yen, K. Sedighiani, P. Thoudden Sukumar, I.R. Souza Filho, S. Katnagallu, E. Jägle, P. Kürnsteiner, N. Kusampudi, L. Stephenson, M. Herbig, C.H. Liebscher, H. Springer, S. Zaeferer, V. Shah, S.-L. Wong, C. Baron, M. Diehl, F. Roters, D. Ponge, Current challenges and opportunities in microstructure-related properties of advanced high-strength steels, *Metall. Mater. Trans. A* 51 (2020) 5517–5586.
- [34] L. Morsdorf, O. Jeannin, D. Barbier, M. Mitsuhara, D. Raabe, C.C. Tasan, Multiple mechanisms of lath martensite plasticity, *Acta Mater.* 121 (2016) 202–214.
- [35] D. Rudomilova, T. Prošek, P. Salvetr, A. Knaislová, P. Novák, R. Kodým, G. Schimo-Aichhorn, A. Muhr, H. Duchaczek, G. Luckeneder, The effect of microstructure on hydrogen permeability of high strength steels, *Mater. Corros.* 71 (2019) 909–917.